

# On-demand formation of Lewis bases for efficient and stable perovskite solar cells

Received: 12 September 2024

Accepted: 7 March 2025

Published online: 17 April 2025

 Check for updates

Sheng Fu <sup>1,7</sup>✉, Nannan Sun<sup>1,7</sup>, Hao Chen <sup>2,7</sup>, Cheng Liu <sup>2,7</sup>, Xiaoming Wang <sup>1</sup>, You Li <sup>1</sup>, Abasi Abudulimu <sup>1</sup>, Yuanze Xu<sup>3</sup>, Shipathi Ramakrishnan <sup>3</sup>, Chongwen Li<sup>2</sup>, Yi Yang <sup>2</sup>, Haoyue Wan <sup>2</sup>, Zixu Huang<sup>4</sup>, Yeming Xian <sup>1</sup>, Yifan Yin<sup>1</sup>, Tingting Zhu<sup>1</sup>, Haoran Chen<sup>1</sup>, Amirhossein Rahimi<sup>1</sup>, Muhammad Mohsin Saeed <sup>1</sup>, Yugang Zhang <sup>5</sup>, Qiuming Yu <sup>3</sup>, David S. Ginger <sup>4</sup>, Randy J. Ellingson <sup>1</sup>, Bin Chen <sup>2</sup>, Zhaoning Song <sup>1</sup>, Mercouri G. Kanatzidis <sup>2</sup>, Edward H. Sargent <sup>2,6</sup>✉ & Yanfa Yan <sup>1</sup>✉

In the fabrication of FAPbI<sub>3</sub>-based perovskite solar cells, Lewis bases play a crucial role in facilitating the formation of the desired photovoltaic  $\alpha$ -phase. However, an inherent contradiction exists in their role: they must strongly bind to stabilize the intermediate  $\delta$ -phase, yet weakly bind for rapid removal to enable phase transition and grain growth. To resolve this conflict, we introduced an on-demand Lewis base molecule formation strategy. This approach utilized Lewis-acid-containing organic salts as synthesis additives, which deprotonated to generate Lewis bases precisely when needed and could be reprotonated back to salts for rapid removal once their role is fulfilled. This method promoted the optimal crystallization of  $\alpha$ -phase FAPbI<sub>3</sub> perovskite films, ensuring the uniform vertical distribution of A-site cations, larger grain sizes and fewer voids at buried interfaces. Perovskite solar cells incorporating semicarbazide hydrochloride achieved an efficiency of 26.1%, with a National Renewable Energy Laboratory-certified quasi-steady-state efficiency of 25.33%. These cells retained 96% of their initial efficiency after 1,000 h of operation at 85 °C under maximum power point tracking. Additionally, mini-modules with an aperture area of 11.52 cm<sup>2</sup> reached an efficiency of 21.47%. This strategy is broadly applicable to all Lewis-acid-containing organic salts with low acid dissociation constants and offers a universal approach to enhance the performance of perovskite solar cells and modules.

State-of-the-art perovskite solar cells (PSCs) and modules utilize formamidinium lead iodide (FAPbI<sub>3</sub>)-based absorbers<sup>1–5</sup>. Achieving high-quality FAPbI<sub>3</sub> photovoltaic films requires lower annealing temperatures to minimize the loss of volatile species such as iodine (I) and formamidinium (FA)<sup>6,7</sup>. However, FAPbI<sub>3</sub> crystallizes into the desired  $\alpha$ -phase—essential for photovoltaics—only at annealing temperatures above 150 °C, whereas lower temperatures lead to the formation of the non-photovoltaic  $\delta$ -phase<sup>2,8</sup>. To facilitate  $\alpha$ -phase formation,

methylammonium chloride (MACl) is often introduced, as the smaller MA<sup>+</sup> cations and Cl<sup>−</sup> anions aid crystallization<sup>9–11</sup>. Unfortunately, incorporating MA into the perovskite lattice compromises the device's thermal stability<sup>12–14</sup>. As an alternative, MA-free FAPbI<sub>3</sub> films commonly integrate inorganic A-site cations such as caesium (Cs) and rubidium (Rb) to enhance film quality and stability<sup>15–18</sup>. However, this approach presents two challenges: reduced film quality—characterized by smaller grain sizes and voids at the buried interface<sup>15,19,20</sup>—and inhomogeneous

A full list of affiliations appears at the end of the paper. ✉ e-mail: [sheng.fu2@utoledo.edu](mailto:sheng.fu2@utoledo.edu); [ted.sargent@northwestern.edu](mailto:ted.sargent@northwestern.edu); [yanfa.yan@utoledo.edu](mailto:yanfa.yan@utoledo.edu)

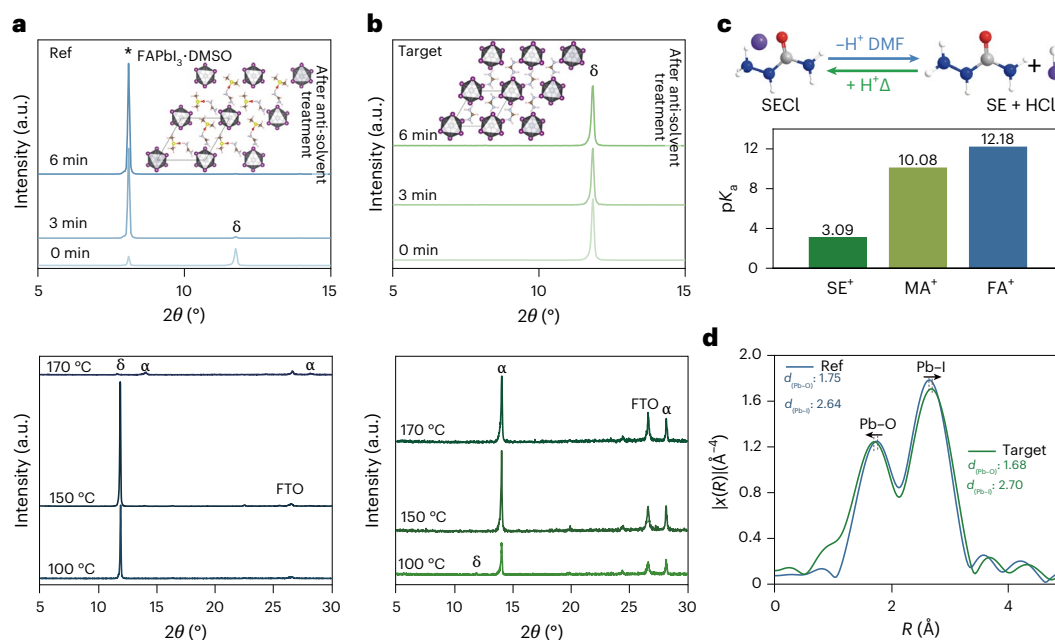


**Fig. 1 | Influence of the on-demand formation of SE molecules on the formation of FAPbI<sub>3</sub> perovskite films. a, b**, XRD patterns of the Ref and Target FAPbI<sub>3</sub> films before (top) and after (bottom) annealing. The images in the inset

illustrate the crystalline structures of FAPbI<sub>3</sub>·DMSO and  $\delta$ -FAPbI<sub>3</sub>. **c**, Reversible deprotonation–protonation processes of the SECl molecule. **d**, Extended X-ray absorption fine structure spectra obtained from Ref and Target precursor films.

vertical distribution of A-site cations due to differing crystallization rates between all-inorganic perovskites (CsPbI<sub>3</sub> and RbPbI<sub>3</sub>) and FAPbI<sub>3</sub> (ref. 16). To address these issues, researchers have explored methods such as seeding homogeneous film formation to mitigate phase separation<sup>14,15</sup> and incorporating the additive 1-(phenylsulfonyl) pyrrole to improve the vertical cation distribution of A-site cations<sup>16</sup>. These strategies have enhanced the vertical distribution of inorganic A-site cations, resulting in higher power conversion efficiency (PCE) and improved PSC stability.

Another approach involves accelerating the transition of FAPbI<sub>3</sub> from the  $\delta$ -phase to the  $\alpha$ -phase<sup>15,21,22</sup>. In perovskite processing, Lewis base molecules coordinate with Pb ions on the surface of the  $\delta$ -phase, and the rapid removal of these molecules (such as dimethylformamide (DMF) and dimethylsulfoxide (DMSO)) has been shown to facilitate this phase transition<sup>23</sup>. However, this method faces a fundamental trade-off: although strong coordination helps stabilize the intermediate  $\delta$ -phase and activates Pb–I bonds, it also slows the extraction process, hindering the rapid transition to the  $\alpha$ -phase<sup>24–28</sup>.

We hypothesized that creating and subsequently eliminating Lewis base molecules on demand could resolve the issue of conflicting requirements. To achieve this, we used semicarbazide hydrochloride (SECl), a Lewis-acid-containing salt that deprotonated to generate semicarbazide (SE) Lewis base molecules. Once their role in the phase transition was complete, these molecules could be rapidly removed by reprotonation, converting them back into salt. This reprotonation process occurred swiftly on solvent removal. The on-demand formation of SE Lewis base molecules facilitated the desirable crystallization of photovoltaic  $\alpha$ -phase FAPbI<sub>3</sub> films, leading to the homogeneous vertical distribution of A-site cations, larger grain sizes and reduced void density at buried interfaces. This strategy significantly enhanced the performance of PSCs, achieving a PCE of 26.12%, with a certified quasi-steady-state PCE of 25.33% at National Renewable Energy Laboratory (NREL)–outperforming PSCs without the SECl additive (23.04%). Furthermore, devices incorporating SECl retained over 96% of their initial efficiency after 1,000 h of maximum power point tracking (MPPT) under simulated AM1.5 illumination at 85 °C. This approach also demonstrated excellent scalability, achieving champion

PCEs of 24.41% for 1.2-cm<sup>2</sup> cells and 21.47% for 11.52-cm<sup>2</sup> (aperture area) mini-modules.

### Influence on phase transition in FAPbI<sub>3</sub> films

We first examined how our strategy influenced the phase transition of pure FAPbI<sub>3</sub> thin films, with the commonly used DMF and DMSO solvents as references for comparison<sup>29–32</sup>. When FAPbI<sub>3</sub> films were processed without SECl (Ref; Fig. 1a, top), the intermediate  $\delta$ -phase initially formed after anti-solvent dripping, exhibiting an X-ray diffraction (XRD) peak at 11.8°. This phase then transitioned into a FAPbI<sub>3</sub>·DMSO intermediate phase due to the presence of residual DMSO molecules, as indicated by the XRD peak at 8.1° (refs. 33,34). Although the exact crystal structure of the FAPbI<sub>3</sub>·DMSO intermediate phase has not been reported, our density functional theory (DFT) calculations suggested that it formed through DMSO diffusion into the  $\delta$ -phase (Fig. 1a (inset); the fitting results are shown in Supplementary Fig. 1). On the surface of the FAPbI<sub>3</sub>·DMSO intermediate phase, DMSO molecules coordinated with Pb ions, whereas inside the structure, they interacted with FA ions via weak Coulombic attraction, with a calculated binding energy of 0.3 eV, due to the lone-pair electrons on the oxygen atoms of DMSO. The lattice parameters shifted from  $a = b = 8.66$  Å and  $c = 7.90$  Å in the intermediate  $\delta$ -phase to  $a = b = 12.20$  Å and  $c = 7.44$  Å in the FAPbI<sub>3</sub>·DMSO intermediate phase.

Incorporating a small amount of SECl additive (1% target) significantly altered the growth process of FAPbI<sub>3</sub> thin films. As shown in the XRD patterns (Fig. 1b, top), the intermediate  $\delta$ -phase formed and remained, even though the precursor contained the same amount of DMSO. This behaviour can be attributed to the much lower acid dissociation constant ( $pK_a$ ) of SE<sup>+</sup> cations compared with MA<sup>+</sup> and FA<sup>+</sup> (Fig. 1c and Supplementary Fig. 2). The  $-\text{NH}_3^+$  group in SE<sup>+</sup> is bonded to the strongly electronegative  $-\text{C}=\text{O}$  group, resulting in weaker proton binding. By contrast, the  $-\text{NH}_3^+$  group in MA<sup>+</sup> and the  $\text{NH}_2^+$  group in FA<sup>+</sup> are bonded to  $-\text{CH}_3$  and  $-\text{C}-\text{N}$  groups, respectively, which are less electronegative. Simulated  $pK_a$  values indicated that SE<sup>+</sup> cations readily deprotonate into SE in DMF- and DMSO-based precursors (Supplementary Fig. 2). On solvent removal, SE molecules reprotonate back to SECl. This reversible deprotonation–protonation

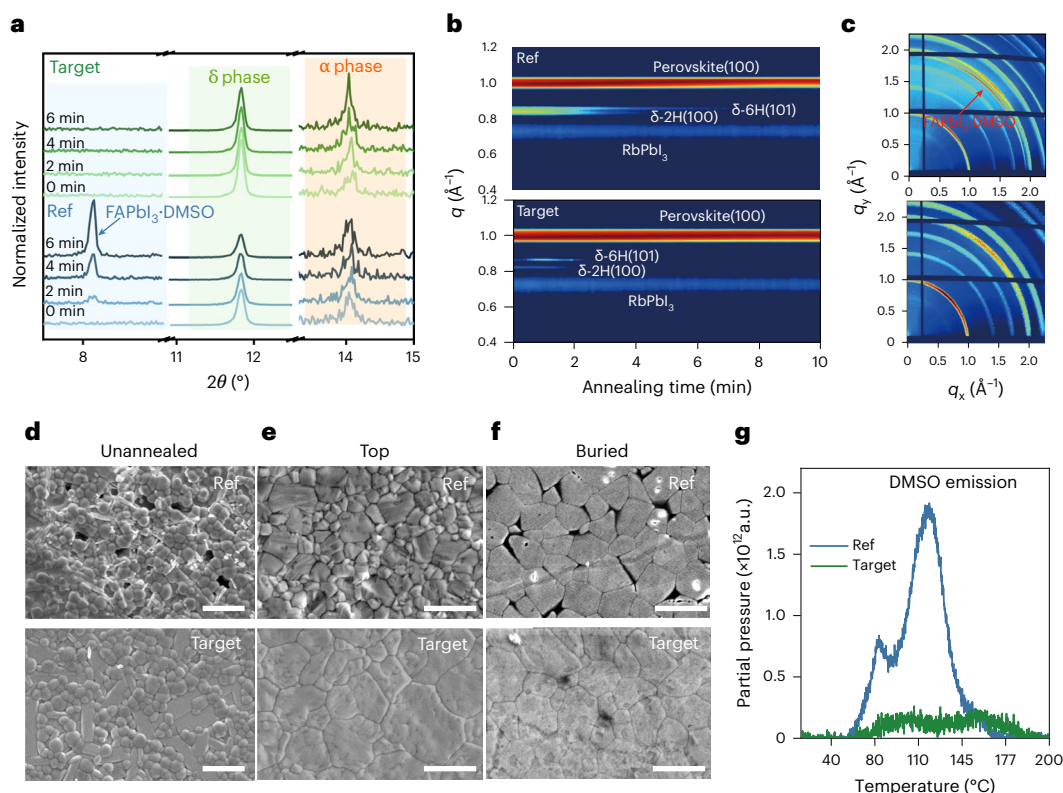


**Fig. 2 | Effects of the on-demand formation of SE molecules on the crystallization of Cs- and Rb-containing perovskite films. a**, In situ XRD patterns of the Ref and Target films after anti-solvent treatments. The intensity for each region is normalized by the highest intensity. **b**, In situ GIWAXS of the

Ref and Target perovskite films during annealing. **c**, GIWAXS patterns of the annealed Ref and Target films. **d–f**, SEM images of the Ref (top) and Target (bottom) films before (**d**) and after (**e** and **f**) annealing. Scale bar, 1  $\mu\text{m}$ . **g**, DMSO signals from the TR-MS measurements of the Ref and Target films.

process was experimentally confirmed via Fourier transform infrared spectroscopy (Supplementary Fig. 3). In SECI powder, a narrow peak corresponding to the  $-\text{NH}_3^+$  group broadened to an  $\text{NH}_2$ -associated peak when dissolved in DMF and then reverted to the narrow peak on DMF removal. DFT calculations further suggested that SE molecules bind more strongly to Pb ions on the surface of the intermediate  $\delta$ -phase than DMSO molecules (Supplementary Fig. 4). This stronger coordination shortens Pb–O bond lengths and extends Pb–I bond lengths, thereby facilitating the phase transition<sup>10</sup>. Extended X-ray absorption fine structure analysis of the Pb L-III edges (Fig. 1d; raw data are shown in Supplementary Fig. 5) further supported this coordination mechanism. The Pb–O bond length decreased from 1.75 Å to 1.68 Å in the presence of SECI, whereas the Pb–I bond length increased from 2.64 Å to 2.70 Å, with a reduction in the Pb–I signal intensity—confirming SE coordination at the  $\delta$ -phase surface. This stronger coordination stabilized the  $\delta$ -phase, preventing DMSO diffusion and thereby inhibiting the formation of the  $\text{FAPbI}_3$ -DMSO intermediate phase. This is consistent with the observation that the  $\delta$ -phase remained intact after anti-solvent dripping.

Next, we investigated the effects of annealing on phase transitions. In the reference sample, the  $\text{FAPbI}_3$ -DMSO intermediate initially reverted to the  $\delta$ -phase on annealing at 100 °C due to the release of strongly coordinated DMSO molecules (Fig. 1a, bottom). Because of this strong coordination, the formation of the  $\alpha$ -phase only occurred after annealing at 170 °C. A possible pathway for this  $\delta$ -to- $\alpha$ -phase transition is illustrated in Supplementary Fig. 6<sup>35</sup>. This delayed transition resulted in poor film quality, as reflected in the XRD data (Fig. 1a, bottom). In sharp contrast, as shown in Fig. 1b (bottom), the Target sample underwent a phase transition as early as 100 °C, producing high-quality  $\alpha$ -phase films with further annealing. On the basis of these findings, we concluded that on annealing, DMF and DMSO evaporated

quickly, leading to the protonation of SE molecules back into SECI salt (Supplementary Fig. 3). This process removed SE molecules from the surface of the intermediate  $\delta$ -phase, thereby accelerating the  $\delta$ -to- $\alpha$ -phase transition at significantly lower temperatures (100 °C instead of 170 °C). Furthermore, SECI remained in the perovskite film due to its thermal stability, as confirmed by Extended Data Fig. 1.

The on-demand formation of SE molecules played a crucial role in facilitating the rapid transition from the  $\delta$ -phase to the  $\alpha$ -phase. If pre-synthesized base molecules were used as additives, they would coordinate with Pb ions on the  $\delta$ -phase surface, requiring higher annealing temperatures for removal. To validate this, we introduced carbonyl diimide (CDI) molecules as an additive<sup>19</sup>, as pre-synthesized SE molecules were unavailable. Since CDI exhibits even stronger coordination with Pb ions than SE (Supplementary Figs. 4 and 7), it further stabilized the intermediate  $\delta$ -phase. Due to this stronger coordination energy, CDI molecules were more difficult to remove during annealing, leading to a residual  $\delta$ -phase even after heating to 170 °C (Supplementary Fig. 7b). By contrast, the reversible reprotonation process of SE molecules depended solely on the concentration of uncoordinated solvents, which evaporated more easily on annealing. This enabled phase transition at lower temperatures. Similar results were observed when using  $\text{CBHCl}_2$  salt as an additive (Supplementary Fig. 8). Thus, the on-demand deprotonation and reprotonation of Lewis base molecule halide salts present an effective strategy to accelerate the  $\delta$ -to- $\alpha$ -phase transition in  $\text{FAPbI}_3$ . This approach helped balance crystallization rates between all-inorganic perovskites and  $\text{FAPbI}_3$ , promoting a more homogeneous vertical distribution of A-site cations.

### Effects on vertical distribution of A-site cations

Previous studies have shown that all-inorganic  $\text{CsPbI}_3$  perovskite crystallizes faster than the organic A-site  $\text{FAPbI}_3$  perovskite<sup>15,16,36</sup>, leading

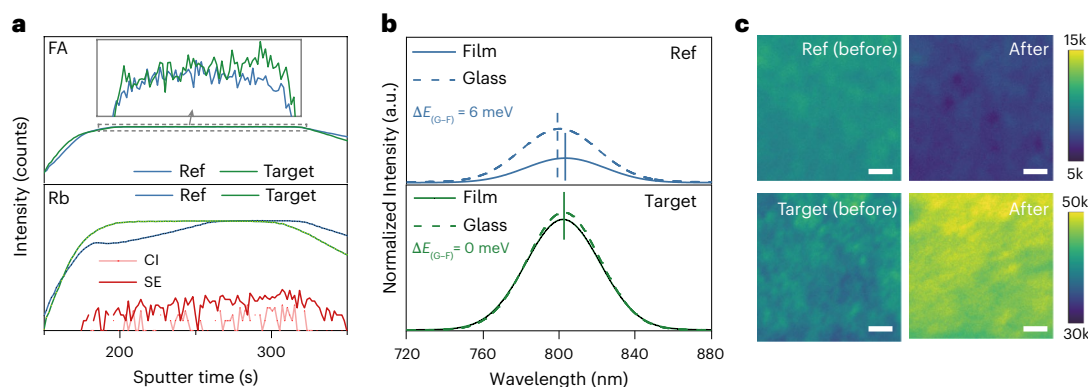


**Fig. 3 | Vertical distribution of A-site cations and film stability.** **a**, TOF-SIMS profiles of the Ref and Target films. **b,c**, PL curves and hyperspectral PL mappings of the Ref and Target films. Scale bar (PL mapping), 10  $\mu\text{m}$ .

to inhomogeneous phase formation. This results in an undesirable vertical gradient, with inorganic A-site cations concentrated at the bottom and organic cations accumulating at the top. To investigate the impact of our on-demand strategy on the vertical distribution of A-site cations, we examined the composition  $\text{FA}_{0.85}\text{MA}_{0.05}\text{Cs}_{0.05}\text{Rb}_{0.05}\text{PbI}_{2.85}\text{Br}_{0.15}$ , a well-established formulation known for its high efficiency in PSCs and its widespread use in research<sup>37–39</sup>. Our findings (Fig. 2a and Supplementary Fig. 9) revealed similar trends to those observed in  $\text{FAPbI}_3$ . In the reference (Ref) films, the intermediate  $\delta$ -phase initially formed and then transitioned to the  $\text{FAPbI}_3$ -DMSO phase. However, in the SECI-treated films (Target), the intermediate  $\delta$ -phase remained stable. The inclusion of Cs and Rb facilitated the formation of a small amount of  $\alpha$ -phase in both Ref and Target samples, probably due to their smaller ionic sizes, which promoted the phase transition.

To investigate the phase formation dynamics during annealing, we conducted in situ grazing-incidence wide-angle X-ray scattering (GIWAXS) measurements. In the Ref film, it took 7 min for the  $\delta$ -phase to disappear (Fig. 2b), whereas in the Target film, this transition occurred in just 2.5 min. The final films exhibited similar absorption spectra (Supplementary Fig. 10) and identical GIWAXS patterns (Fig. 2c), both displaying the  $\delta$ - $\text{RbPbI}_3$  GIWAXS signature at  $0.73 \text{ \AA}^{-1}$ . Since SECI did not alter the perovskite film's bandgap, we concluded that it was not incorporated into the perovskite lattice. In particular, the diffraction rings of the (100) plane at  $1.0 \text{ \AA}^{-1}$  showed a stronger intensity in the Target film, whereas the Ref film retained a ring corresponding to the  $\text{FAPbI}_3$ -DMSO phase before and after annealing (Supplementary Fig. 11 and Fig. 2c). The weak ring in the Ref film after annealing suggested that DMSO molecules were not fully removed at  $100 \text{ }^\circ\text{C}$ . Additionally, the Target film exhibited improved morphology (Fig. 2d–f), in contrast to the Ref film, which contained horizontal grain boundaries (Supplementary Fig. 12). The absence of voids in the Target film correlates with the efficient removal of DMSO<sup>19,40,41</sup>, as further confirmed by temperature-resolved mass spectroscopy (TR-MS). In the Ref film, a strong DMSO emission was detected even above  $140 \text{ }^\circ\text{C}$  (Fig. 2g), whereas in the Target film, only a weak DMSO signal was observed. The optimal SECI concentration was determined to be  $2 \text{ mg ml}^{-1}$  (Extended Data Fig. 2).

The depth distributions of elements and phases in the annealed perovskite films were analysed using grazing-incidence XRD with incident-angle scanning (Supplementary Fig. 14) and time-of-flight secondary ion mass spectrometry (TOF-SIMS; Supplementary Fig. 15). The grazing-incidence XRD results revealed that in the Ref film, Rb was concentrated at the bottom interface but deficient at the top surface, whereas the Target film exhibited a more homogeneous Rb distribution. These findings aligned with the TOF-SIMS depth profiles (Fig. 3a, bottom), which showed a higher Rb concentration near the buried interface in the Ref film but a more uniform vertical distribution in the Target film. Moreover, the SECI signals in the Target film appeared

evenly distributed (Fig. 3a, bottom), contributing to effective grain and surface modulations, as reflected by the  $\text{Pb}4f$  and  $\text{I}3d$  X-ray photoelectron spectroscopy chemical shifts (Extended Data Fig. 3)<sup>42,43</sup>. To further examine the vertical A-site cation distribution, we analysed the FA cation profile, as Cs was the reference source for the TOF-SIMS measurement. The FA depth profile (Fig. 3a, top) showed a lower signal intensity near the buried interface in the Ref film, indicating Cs accumulation in this region. The X-ray photoelectron spectroscopy depth profiles (Extended Data Fig. 4) further confirmed the vertical regulation of A-site cations by SECI. Although the Ref film exhibited higher Cs and Rb concentrations in the bottom region, the Target film displayed a more uniform distribution of these cations. This improved homogeneity in the Target film also explains the photoluminescence (PL) results obtained from glass- and film-side measurements (Fig. 3b). In the Ref film, the glass-side emission showed a 6-meV higher energy than the film-side emission, whereas in the Target film, no energy difference was observed between the two sides.

The time-resolved PL spectra revealed longer carrier lifetimes in the Target film compared with the Ref film (Supplementary Fig. 16). Additionally, the PL intensity and PL quantum yield in the Ref film were higher when measured from the glass side than from the film side (Supplementary Fig. 17 and Fig. 3b). This observation aligned with the inhomogeneous vertical distribution of  $\text{RbPbI}_3$ , where  $\text{RbPbI}_3$  preferentially accumulated near the buried interface in the Ref film. By contrast, the Target film exhibited a much smaller difference between the glass-side and film-side PL measurements, indicating a more uniform vertical distribution of  $\text{RbPbI}_3$ . Reducing voids at the buried interface is expected to improve hole extraction at the hole-transporting layer–perovskite interface in the p–i–n solar cell<sup>44–46</sup>, a result further supported by the transient photovoltage measurements of bifacial PSCs fabricated with the Ref and Target perovskite films (Supplementary Fig. 18). Furthermore, space-charge-limited current measurements (Supplementary Fig. 19) revealed a significant reduction in trap density, decreasing from  $3.58 \times 10^{15} \text{ cm}^{-3}$  in the Ref film to  $2.15 \times 10^{15} \text{ cm}^{-3}$  in the Target film.

We used hyperspectral PL imaging to assess the stability of the Ref and Target films under 1-sun 532-nm laser illumination (Supplementary Fig. 20). As shown in Fig. 3c, the Ref film displayed a significant decrease in intensity after exposure, whereas the Target film remained unchanged, exhibiting no signs of degradation (Extended Data Fig. 5).

## Device performance

We constructed p–i–n inverted solar cells (Fig. 4a and Supplementary Table 1) with the architecture F-doped tin oxide (FTO)/2-(3,6-dimethoxycarbazol-9-yl)ethylphosphonic acid (MeO-2PACz)/perovskite/fullerene ( $\text{C}_{60}$ )/bathocuproine (BCP)/Ag, utilizing a perovskite composition of  $\text{FA}_{0.85}\text{MA}_{0.05}\text{Cs}_{0.05}\text{Rb}_{0.05}\text{PbI}_{2.85}\text{Br}_{0.15}$ . The perovskite layer had a thickness of approximately 760 nm (the cross-sectional

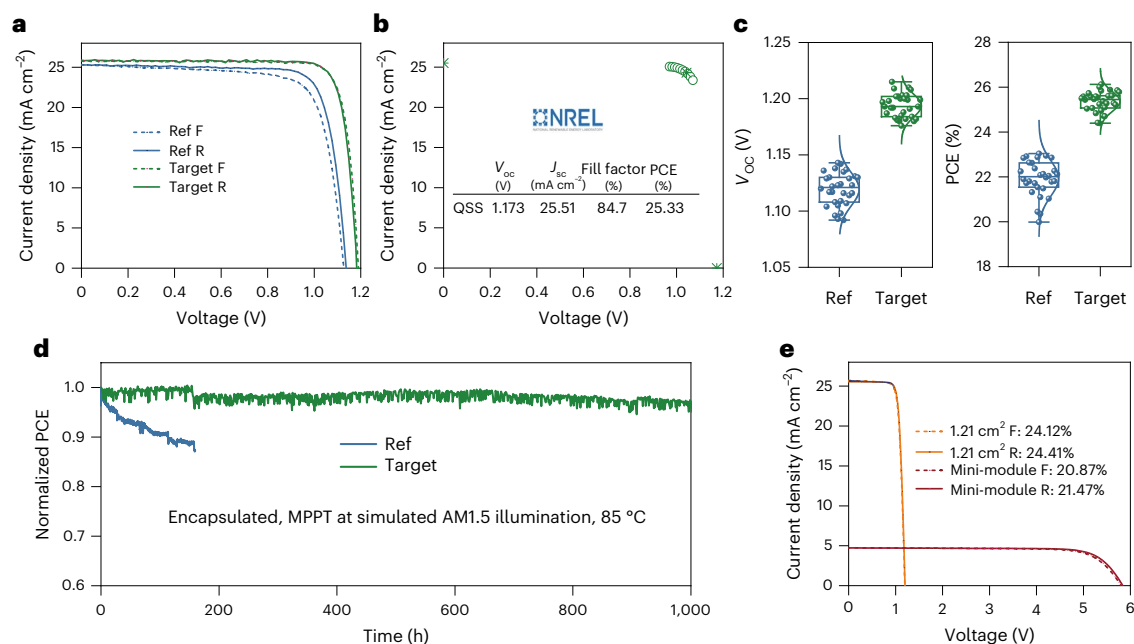


**Fig. 4 | Impact of the on-demand formation of SE molecules on device performance.** **a, b,**  $J$ - $V$  curves of the champion Ref and Target PSCs (**a**) and the quasi-steady-state (QSS) curve certified by NREL (**b**) of the champion Ref and Target PSCs. **c,** Statistical diagrams of the  $V_{oc}$  and PCE values of the Ref and Target devices (30 individual samples; whiskers, minimum value for lower and

maximum value for upper; bounds of box: 25th and 75th percentiles; centre: mean). **d,** MPPT stability of the PSCs at 85 °C. **e,**  $J$ - $V$  curves of the champion efficiency for large-area devices and mini-modules. Credit: **b,** National Renewable Energy Laboratory.

scanning electron microscopy (SEM) image is shown in Supplementary Fig. 21). The  $J$ - $V$  curves and detailed parameter optimizations are shown in Extended Data Fig. 6 and Supplementary Table 1. The Ref device achieved a PCE of 23.04% (reverse scan (R))/21.57% (forward scan (F)), whereas the Target device (2 mg ml<sup>-1</sup> SECl) exhibited a champion PCE of 26.12% (R)/25.9% (F). The measured short-circuit current densities ( $J_{sc}$ ) of both devices closely aligned with the values integrated from the external quantum efficiency (EQE) spectra (Supplementary Fig. 22), yielding 24.91 mA cm<sup>-2</sup> for the Ref device and 25.32 mA cm<sup>-2</sup> for the Target device. Additionally, an independent measurement of the Target device at the NREL confirmed a certified quasi-steady-state efficiency of 25.33% (Fig. 4b; the certificate is shown in Supplementary Fig. 23).

Figure 4c presents the statistical distributions of the  $V_{oc}$  values and PCEs for 30 individual Ref and Target devices, whereas the distributions of  $J_{sc}$  and fill factor are shown in Supplementary Fig. 24. The Target devices demonstrated consistent improvements across all the photovoltaic parameters compared with the Ref devices. In particular, the Target devices achieved a maximum  $V_{oc}$  of 1.215 V (Supplementary Fig. 25), resulting in a  $V_{oc}$  deficit of just 0.325 V, among the lowest reported values for inverted PSCs (Supplementary Table 2). Additionally, the incorporation of CBHCl<sub>2</sub> also enhanced the photovoltaic performance, yielding an efficiency of 25%, compared with 24.4% with lower CBH concentrations (Extended Data Fig. 7). To assess whether the on-demand formation strategy could also improve the vertical distribution of A-site cations in other perovskite compositions, we investigated FA<sub>0.95</sub>CS<sub>0.05</sub>PbI<sub>3</sub> and FA<sub>0.9</sub>CS<sub>0.1</sub>PbI<sub>3</sub>, both of which exhibited the same homogenization trend (Supplementary Fig. 26).

We evaluated the stability of encapsulated Ref and Target devices under MPPT with continuous simulated AM1.5 illumination under ambient conditions (Supplementary Fig. 27). The Ref device exhibited rapid degradation, with its PCE dropping below 80% of its initial value after 1,000 h of MPPT. By contrast, the Target device maintained its initial PCE even after 3,000 h of MPPT. Additionally, an encapsulated Target device retained 96% of its initial efficiency after 1,000 h of MPPT under simulated AM1.5 illumination at 85 °C (Fig. 4d). By comparison, the Ref

device degraded to 90% of its initial PCE within just 100 h under the same conditions. The enhanced photothermal stability of the Target device can be attributed to the homogeneous vertical distribution of A-site cations and its higher crystallinity.

We explored the initial scaling of PSC fabrication and mini-module development. A 1.21-cm<sup>2</sup> device achieved a champion PCE of 24.41% with a  $V_{oc}$  of 1.2 V (Fig. 4e, yellow curves; statistical data and EQE curve are shown in Supplementary Figs. 28 and 29). For mini-modules, we fabricated mini-modules on 5 × 5 cm<sup>2</sup> substrates containing five subcells with a geometric fill factor of 94.8% (Supplementary Fig. 30), demonstrating good reproducibility (Supplementary Fig. 31). The champion mini-module delivered a PCE of 21.47% (Fig. 4e) with an aperture area of 11.52 cm<sup>2</sup> and an active-area efficiency of 22.65%. Both the large-area device and mini-module retained 98% of their initial PCEs after 1,000 h of MPPT under ambient conditions (Supplementary Fig. 32).

## Conclusion

We have introduced and demonstrated that the on-demand formation of Lewis base molecules is an effective strategy to facilitate the transition from the  $\delta$ -phase to the  $\alpha$ -phase in FAPbI<sub>3</sub> perovskite. The key mechanism behind this process involves deprotonation and reprotonation, which accelerates the formation of  $\alpha$ -phase FAPbI<sub>3</sub> and prevents the preferential formation of the  $\delta$ -phases of CsPbI<sub>3</sub> and RbPbI<sub>3</sub>. Rb ions diffuse outwards during annealing, forming RbPbI<sub>3</sub> at the grain surfaces, film surfaces, grain boundaries and buried interfaces, ultimately achieving a homogeneous vertical distribution. This uniform A-site cation distribution and larger grain sizes would significantly enhance solar cell performance.

## Online content

Any methods, additional references, Nature Portfolio reporting summaries, source data, extended data, supplementary information, acknowledgements, peer review information; details of author contributions and competing interests; and statements of data and code availability are available at <https://doi.org/10.1038/s41565-025-01900-9>.

## References

1. Park, J. et al. Controlled growth of perovskite layers with volatile alkylammonium chlorides. *Nature* **616**, 724–730 (2023).
2. Hui, W. et al. Stabilizing black-phase formamidinium perovskite formation at room temperature and high humidity. *Science* **371**, 1359–1364 (2021).
3. Chen, H. et al. Improved charge extraction in inverted perovskite solar cells with dual-site-binding ligands. *Science* **384**, 189–193 (2024).
4. Li, X. et al. Constructing heterojunctions by surface sulfidation for efficient inverted perovskite solar cells. *Science* **375**, 434–437 (2022).
5. Jiang, Q. et al. Surface reaction for efficient and stable inverted perovskite solar cells. *Nature* **611**, 278–283 (2022).
6. Chen, R. et al. Reduction of bulk and surface defects in inverted methylammonium- and bromide-free formamidinium perovskite solar cells. *Nat. Energy* **8**, 839–849 (2023).
7. Hou, T. et al. Methylammonium-free ink for low-temperature crystallization of  $\alpha$ -FAPbI<sub>3</sub> perovskite. *Adv. Energy Mater.* **14**, 2400932 (2024).
8. Jeong, J. et al. Pseudo-halide anion engineering for  $\alpha$ -FAPbI<sub>3</sub> perovskite solar cells. *Nature* **592**, 381–385 (2021).
9. Kim, M. et al. Methylammonium chloride induces intermediate phase stabilization for efficient perovskite solar cells. *Joule* **3**, 2179–2192 (2019).
10. Niu, T. et al. Phase-pure  $\alpha$ -FAPbI<sub>3</sub> perovskite solar cells via activating lead-iodine frameworks. *Adv. Mater.* **36**, e2309171 (2023).
11. Chao, L. et al. Direct and stable  $\alpha$ -phase formation via ionic liquid solvation for formamidinium-based perovskite solar cells. *Joule* **6**, 2203–2217 (2022).
12. Liu, C., Cheng, Y. B. & Ge, Z. Understanding of perovskite crystal growth and film formation in scalable deposition processes. *Chem. Soc. Rev.* **49**, 1653–1687 (2020).
13. Castro-Mendez, A. F. et al. Tailoring interface energies via phosphonic acids to grow and stabilize cubic FAPbI<sub>3</sub> deposited by thermal evaporation. *J. Am. Chem. Soc.* **14**, 18459–18469 (2024).
14. Sidhik, S. et al. Two-dimensional perovskite templates for durable, efficient formamidinium perovskite solar cells. *Science* **384**, 1227–1235 (2024).
15. Bai, Y. et al. Initializing film homogeneity to retard phase segregation for stable perovskite solar cells. *Science* **378**, 747–754 (2022).
16. Liang, Z. et al. Homogenizing out-of-plane cation composition in perovskite solar cells. *Nature* **624**, 557–563 (2023).
17. Chen, H. et al. Quantum-size-tuned heterostructures enable efficient and stable inverted perovskite solar cells. *Nat. Photon.* **16**, 352–358 (2022).
18. Jiang, Q. et al. Surface passivation of perovskite film for efficient solar cells. *Nat. Photon.* **13**, 460–466 (2019).
19. Chen, S. et al. Stabilizing perovskite-substrate interfaces for high-performance perovskite modules. *Science* **373**, 902–907 (2021).
20. Bu, T. et al. Lead halide-templated crystallization of methylamine-free perovskite for efficient photovoltaic modules. *Science* **372**, 1327–1332 (2021).
21. Lu, H. et al. Vapor-assisted deposition of highly efficient, stable black-phase FAPbI<sub>3</sub> perovskite solar cells. *Science* **370**, eabb8985 (2020).
22. Xu, Z. et al. Reducing energy barrier of  $\delta$ -to- $\alpha$  phase transition for printed formamidinium lead iodide photovoltaic devices. *Nano Energy* **91**, 106658 (2022).
23. Huang, X. et al. Solvent gaming chemistry to control the quality of halide perovskite thin films for photovoltaics. *ACS Cent. Sci.* **8**, 1008–1016 (2022).
24. Huang, Z. et al. Anion- $\pi$  interactions suppress phase impurities in FAPbI<sub>3</sub> solar cells. *Nature* **623**, 531–537 (2023).
25. Sun, N. et al. Tailoring crystallization dynamics of CsPbI<sub>3</sub> for scalable production of efficient inorganic perovskite solar cells. *Adv. Funct. Mater.* **34**, 2309894 (2023).
26. Xu, J. et al. Anion optimization for bifunctional surface passivation in perovskite solar cells. *Nat. Mater.* **22**, 1507–1514 (2023).
27. Li, C. et al. Rational design of Lewis base molecules for stable and efficient inverted perovskite solar cells. *Science* **379**, 690–694 (2023).
28. Fu, S. et al. Efficient passivation with lead pyridine-2-carboxylic for high-performance and stable perovskite solar cells. *Adv. Energy Mater.* **9**, 1901852 (2019).
29. Azmi, R. et al. Double-side 2-dimensional/3-dimensional heterojunctions for inverted perovskite solar cells. *Nature* **628**, 93–98 (2024).
30. Peng, W. et al. Reducing nonradiative recombination in perovskite solar cells with a porous insulator contact. *Science* **379**, 683–690 (2023).
31. Zhang, S. et al. Minimizing buried interfacial defects for efficient inverted perovskite solar cells. *Science* **380**, 404–409 (2023).
32. Wang, M. et al. Ammonium cations with high pK<sub>a</sub> in perovskite solar cells for improved high-temperature photostability. *Nat. Energy* **8**, 1229–1239 (2023).
33. Du, X. et al. Synergistic crystallization and passivation by a single molecular additive for high-performance perovskite solar cells. *Adv. Mater.* **34**, e2204098 (2022).
34. Zheng, Y. et al. Dual-interface modification for inverted methylammonium-free perovskite solar cells of 25.35% efficiency with balanced crystallization. *Adv. Energy Mater.* **14**, 2304486 (2024).
35. Chen, T. et al. Entropy-driven structural transition and kinetic trapping in formamidinium lead iodide perovskite. *Sci. Adv.* **2**, e1601650 (2016).
36. Kim, H. S. et al. Vacuum-assisted reforming cathode interlayer orientation for efficient and stable perovskite solar cells. *Nano Energy* **125**, 109584 (2024).
37. Chen, P. et al. Multifunctional ytterbium oxide buffer for perovskite solar cells. *Nature* **625**, 516–522 (2024).
38. Duan, T. et al. Chiral-structured heterointerfaces enable durable perovskite solar cells. *Science* **384**, 878–884 (2024).
39. Li, Z. et al. Organometallic-functionalized interfaces for highly efficient inverted perovskite solar cells. *Science* **376**, 416–420 (2022).
40. Wang, M., Fei, C., Uddin, M. A. & Huang, J. Influence of voids on the thermal and light stability of perovskite solar cells. *Sci. Adv.* **8**, eabo5977 (2022).
41. Fu, S. et al. Suppressed deprotonation enables a durable buried interface in tin-lead perovskite for all-perovskite tandem solar cells. *Joule* **8**, 2220–2237 (2024).
42. Zhong, L. et al. Solid additive delicately controls morphology formation and enables high-performance in organic solar cells. *Adv. Funct. Mater.* **33**, 202305450 (2023).
43. Park, J. et al. Triadic halobenzene processing additive combined advantages of both solvent and solid types for efficient and stable organic solar cells. *Small* **20**, e2405415 (2024).
44. He, R. et al. Improving interface quality for 1-cm<sup>2</sup> all-perovskite tandem solar cells. *Nature* **618**, 80–86 (2023).
45. Wu, X. et al. Backbone engineering enables highly efficient polymer hole-transporting materials for inverted perovskite solar cells. *Adv. Mater.* **35**, e2208431 (2023).
46. Yang, W. et al. Unlocking voltage potentials of mixed-halide perovskite solar cells via phase segregation suppression. *Adv. Funct. Mater.* **32**, 2110698 (2021).

**Publisher's note** Springer Nature remains neutral with regard to jurisdictional claims in published maps and institutional affiliations.

Springer Nature or its licensor (e.g. a society or other partner) holds exclusive rights to this article under a publishing agreement with

the author(s) or other rightsholder(s); author self-archiving of the accepted manuscript version of this article is solely governed by the terms of such publishing agreement and applicable law.

© The Author(s), under exclusive licence to Springer Nature Limited 2025

---

<sup>1</sup>Department of Physics and Astronomy and Wright Center for Photovoltaics Innovation and Commercialization, University of Toledo, Toledo, OH, USA.

<sup>2</sup>Department of Chemistry, Northwestern University, Evanston, IL, USA. <sup>3</sup>Robert Frederick Smith School of Chemical and Biomolecular Engineering, Cornell University, Ithaca, NY, USA. <sup>4</sup>Department of Chemistry, University of Washington, Seattle, WA, USA. <sup>5</sup>Center for Functional Nanomaterials, Brookhaven National Laboratory, Upton, NY, USA. <sup>6</sup>Department of Electrical and Computer Engineering, Northwestern University, Evanston, IL, USA.

<sup>7</sup>These authors contributed equally: Sheng Fu, Nannan Sun, Hao Chen, Cheng Liu. ✉ e-mail: [sheng.fu2@utoledo.edu](mailto:sheng.fu2@utoledo.edu); [ted.sargent@northwestern.edu](mailto:ted.sargent@northwestern.edu); [yanfa.yan@utoledo.edu](mailto:yanfa.yan@utoledo.edu)

## Methods

### Materials

The organic halide salts for perovskite precursors, such as methylammonium bromine and formamidinium iodide, were ordered from Greatcell Solar. The powders of lead iodide, lead bromine, caesium iodide, BCP, 1,3-propane-diammonium iodide and MeO-2PACz were purchased from TCI. The solvents (DMF, DMSO, ethanol, chlorobenzene and isopropyl alcohol), rubidium iodide, CBH and SECI were bought from Sigma-Aldrich.  $C_{60}$  was obtained from Nano-C. Tetrakis(dimethylamino) tin(IV) (50-1815 tin) for the atomic layer deposition of  $SnO_2$  was purchased from Strem Chemicals.

### FAPbI<sub>3</sub> film preparation

The FAPbI<sub>3</sub> precursors were prepared by dissolving formamidinium iodide and lead iodide into DMF:DMSO (volume ratio, 4:1) at a concentration of 1 M. The SECI (3 mg ml<sup>-1</sup>) and CBH (2.4 mg ml<sup>-1</sup>) are introduced at the same molar amount. The FAPbI<sub>3</sub> films were spin coated on FTO substrates with the spin procedure of 2,000 rpm for 30 s and 150- $\mu$ l chlorobenzene (CB) anti-solvent treatment at 20 s, following different annealing temperatures for 10 min. The wet FAPbI<sub>3</sub> films were coated into a glovebox and transferred to XRD stages within 1 min.

### Device fabrication

The FTO (size: 2.5 × 2.5 cm<sup>2</sup>) substrates were ultrasonically cleaned successively using Micro-90, water, acetone and isopropyl alcohol for 15 min. Before the coating processes, the FTO glasses were exposed to ultraviolet (UV)-ozone for 30 min for better wettability. Then, MeO-2PACz (0.5 mg ml<sup>-1</sup> in ethanol) hole-transporting layers were spin coated on FTO at a spin speed of 3,000 rpm for 30 s in a glovebox, and annealed at 100 °C for 10 min. After cooling, a 50- $\mu$ l perovskite precursor was dropped on the substrate and coated at 1,000 rpm for 10 s and 4,000 rpm for 40 s. Then, 150  $\mu$ l chlorobenzene as the anti-solvent was dropped on the wet films before 10 s from the end of the coating procedures. Then, the films were annealed at 100 °C for 15 min to complete the phase transition and grain growth. The perovskite precursors (Ref, 1.5 M) were prepared according to the literature<sup>5</sup>. The SECI was directly added into the precursor with different concentrations. The precursors were filtered with a 0.22- $\mu$ m polytetrafluoroethylene membrane before use. As mentioned previously<sup>5</sup>, the precursor could be usable within 1 month. After annealing, 1,3-propane-diammonium iodide (0.3 mg ml<sup>-1</sup> in isopropyl alcohol) was used for surface passivation on the perovskite at a spin speed of 4,500 rpm for 30 s, followed by annealing at 100 °C for 5 min. Finally, the substrates were transferred into a vacuum chamber to evaporate 25-nm  $C_{60}$ , 6-nm BCP and 130-nm Ag. To measure MPPT stability at 85 °C, three changes were made: (1) very thin VNPB layer (0.5 mg ml<sup>-1</sup> in CB, coated at 6,000 rpm for 30 s) was inserted between MeO-2PACz and perovskite; (2) BCP was replaced by 25-nm atomic-layer-deposited  $C_{60}$ ; (3) the Ag electrode was changed into 80-nm Au. The bifacial structure was prepared via sputtering 150-nm indium zinc oxide on an atomic-layer-deposited  $SnO_2$  layer. For mini-module fabrication, the FTO substrates (5 × 5 cm<sup>2</sup>) were first scribed with P1 lines with laser, and the deposition procedures were the same as above. The P2 and P3 lines were scribed before and after Ag evaporation, respectively. Before the  $J$ - $V$  measurements, the modules were heated at 100 °C for 2 min to remove the adsorbed water.

### Characteristics of films and devices

The UV-vis spectra were recorded on a PerkinElmer Lambda 1050 device with a scanning region of 250 nm to 800 nm at a 2-nm step. The thermogravimetry analysis (TG) of SECI powder was conducted on TGA/SDTA851e and the temperature scanning was performed from 25 °C to 300 °C with a step of 5 °C min<sup>-1</sup> under a N<sub>2</sub> flow rate of 30 ml min<sup>-1</sup>. The XRD patterns of the perovskite films were collected using a Rigaku

Ultima-III instrument with Cu K $\alpha$  X-ray source illumination. The Fourier transform infrared spectroscopy data of the powders and solution were obtained using a neaSNOM-nanoFTIR device with potassium bromide tablet carriers. The X-ray absorption fine structure spectra of Pb L-III edge (13,035 eV) were obtained on the as-coated wet FAPbI<sub>3</sub> films using the same parameters as the literature<sup>47</sup>. The electron-beam energy of the storage ring was 3.5 GeV with the maximum stored current of 300 mA. The extended X-ray absorption fine structure spectra were fitted based on the raw data with ATHENA and ARTEMIS software (version 0.9.26). The GIWAXS data were taken at the Complex Materials Scattering (11-BM) beamline of the National Synchrotron Light Source II, Brookhaven National Laboratory. The spin-coating and annealing procedures were the same as the device fabrication, and the difference was that all the operations were performed under ambient conditions (relative humidity, 40%). The samples for annealing were transferred from the spin coater to a hotplate (room temperature) within 10 s. It totally took 14 min for the alignments for detecting the planar substrates (10 min) and preheating to 100 °C (4 min), and we started to collect the GIWAXS images after aligning. The TOF-SIMS measurements were performed on TOF-SIMS V (ION TOF) with a beam of Cs<sup>+</sup> at an energy of 1 keV on an area of 200 × 200  $\mu$ m<sup>2</sup>. The SEM images were collected on Hitachi S-4800 at a scanning voltage of 4 kV. The samples for the top-view and cross-section SEM measurements were coated on indium tin oxide. The TR-MS measurements of the perovskite films were performed at the custom-built temperature programmed desorption (TPD) system. Before heating and signal detection, the chamber with the sample should be vacuumed for 12 h (dark condition) to remove the residual gas. The PL and time-resolved PL data were recorded on a custom-built system with a Horiba Symphony-II charge-coupled device detector/Horiba iHR 320 and Becke & Hickl time-correlated single-photon counting (HPM100-10 and SPM130), respectively. The hyperspectral PL tests were conducted on photons<sup>27</sup>. The 532-nm laser was used as the light source with an intensity of 1 sun. The X-ray photoelectron spectroscopy depth profiles of the films were measured on a Kratos AXIS ULTRA system. The PL quantum yield data were obtained from the integrating sphere with a pre-calibrated fibre coupled to a spectrometer (Ocean Optics QE Pro) with an intensity of ~300 mW cm<sup>-2</sup>. The films were encapsulated with UV epoxy and cover glass before measuring. The transient photovoltages were measured from both sides of the bifacial PSCs with PicoScope 6454 controlled by a custom-built Python code. The devices were encapsulated by UV epoxy and ultrathin glasses. The  $J$ - $V$  curves of the devices were recorded using Keithley 2400 with the AM1.5 solar irradiation (G20 Company). The test procedure is to scan from -0.2 V to 1.4 V at a rate of 100 mV s<sup>-1</sup>. The areas of the devices are defined by the overlapping areas of Ag and FTO substrates, and 0.049-cm<sup>2</sup> and 1.21-cm<sup>2</sup> masks were used to define the aperture area for the  $J$ - $V$  measurements. The EQE spectra of the corresponding devices were obtained from the IVQE8-C model (PV Measurements) to quantify the  $J_{sc}$ . The spectra of the solar simulator and EQE equipment were calibrated using standard solar cells (certified by NREL). The MPP tracking of the unit cells, large area and mini-module were tested at a custom-built system comprising the Keithley 2400 system and under simulated AM1.5 illumination. The temperature around the devices was around 35 °C. The high-temperature MPPT stability of the devices was measured on an oven with the temperature controlled at 85 °C.

### DFT calculations

DFT calculations were performed using the Vienna ab initio simulation package with projector augmented wave potentials<sup>48</sup>. A plane-wave energy cut-off of 500 eV and a  $\Gamma$ -centred 2 × 2 × 2  $k$ -mesh were used for the calculations. The exchange-correlation interactions were treated with the generalized gradient approximation of the Perdew-Burke-Ernzerhof parameterization<sup>49</sup>. Grimme's D3 correction were also included to deal with the van der Waals interactions<sup>50</sup>.

### Reporting summary

Further information on research design is available in the Nature Portfolio Reporting Summary linked to this article.

### Data availability

The main data supporting the findings of this study are available in the Article and its Supplementary Information. Additional data are available from the corresponding authors on reasonable request.

### References

47. Liang, C. et al. Two-dimensional Ruddlesden–Popper layered perovskite solar cells based on phase-pure thin films. *Nat. Energy* **6**, 38–45 (2020).
48. Kresse, G. & Furthmüller, J. Efficient iterative schemes for ab initio total-energy calculations using a plane-wave basis set. *Phys. Rev. B* **54**, 11169–11186 (1996).
49. Perdew, J. P., Burke, K. & Ernzerhof, M. Generalized gradient approximation made simple. *Phys. Rev. Lett.* **77**, 3865–3868 (1996).
50. Grimme, S. et al. A consistent and accurate ab initio parametrization of density functional dispersion correction (DFT-D) for the 94 elements H–Pu. *J. Chem. Phys.* **132**, 154104 (2010).

### Acknowledgements

This material is based on work supported by the US Department of Energy’s Office of Energy Efficiency and Renewable Energy (EERE) under the Solar Energy Technologies Office award no. DE-EE0008970 and under Hydrogen and Fuel Cell Technologies Office award nos. DE-EE0008837 and DE-EE0010740, and by the US Air Force Research Laboratory under agreement no. FA9453-19-C-1002. We also acknowledge support on the DFT calculations from the Center for Hybrid Organic–Inorganic Semiconductors for Energy (CHOISE), an Energy Frontier Research Center funded by the Office of Basic Energy Sciences, Office of Science, US Department of Energy. The DFT calculations are performed using computational resources sponsored by the US Department of Energy’s Office of Energy Efficiency and Renewable Energy located at the National Renewable Energy Laboratory, also using resources of the National Energy Research Scientific Computing Center (NERSC), a US Department of Energy, Office of Science User Facility, located at Lawrence Berkeley National Laboratory, operated under contract no. DE-AC02-05CH11231 using NERSC award no. BES-ERCA0017591. This work was partially

supported by award no. 70NANB19H005 from the US Department of Commerce, National Institute of Standards and Technology, as part of the Center for Hierarchical Materials Design (CHiMaD). The views expressed in the Article do not necessarily represent the views of the Department of Energy or the US Government.

### Author contributions

Y. Yan and S.F. conceived the strategy. Y. Yan supervised the projects and processes. S.F. and N.S. fabricated the devices. S.F., N.S., H.C. and C. Liu conducted the film fabrications and characterizations. X.W. and Y. Xian performed the DFT simulations. A.A. and R.J.E. performed the PL, time-resolved PL and transient photovoltage measurements. Y.L. performed the stability tests. Y. Xu, S.R., Q.Y., Y. Yin and Y.Z. conducted the GIWAXS measurements and data analysis. T.Z. and Haoran Chen collected the XRD data. A.R. and M.M.S. participated in the module fabrications. C. Li, Y. Yang and H.W. measured the TOF-SIMS depth profiles. Z.H. and D.S.G. performed the hyperspectral PL mapping measurements. Z.S. performed the TR-MS measurement. S.F., N.S. and Y. Yan wrote the first draft of the manuscript. S.F., B.C., Z.S., M.G.K., E.H.S. and Y. Yan edited the manuscript. All authors discussed and contributed to the revision of the manuscript.

### Competing interests

Y. Yan and S.F. are authors of a provisional patent (NI2713-004 U, USA) based on this manuscript. The other authors declare no competing interests.

### Additional information

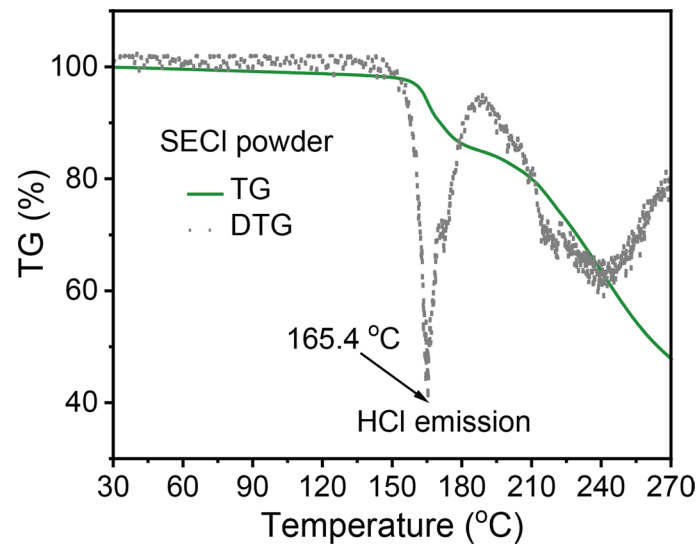
**Extended data** is available for this paper at <https://doi.org/10.1038/s41565-025-01900-9>.

**Supplementary information** The online version contains supplementary material available at <https://doi.org/10.1038/s41565-025-01900-9>.

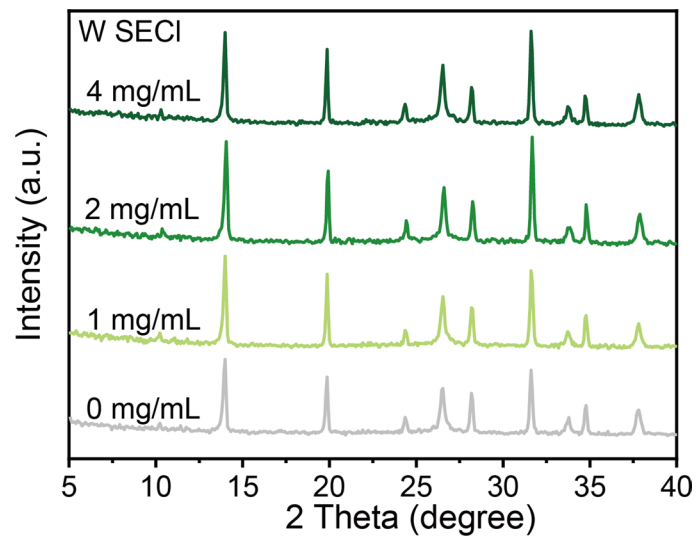
**Correspondence and requests for materials** should be addressed to Sheng Fu, Edward H. Sargent or Yanfa Yan.

**Peer review information** *Nature Nanotechnology* thanks Yongzhen Wu, Changduk Yang, Zonglong Zhu and the other, anonymous, reviewer(s) for their contribution to the peer review of this work.

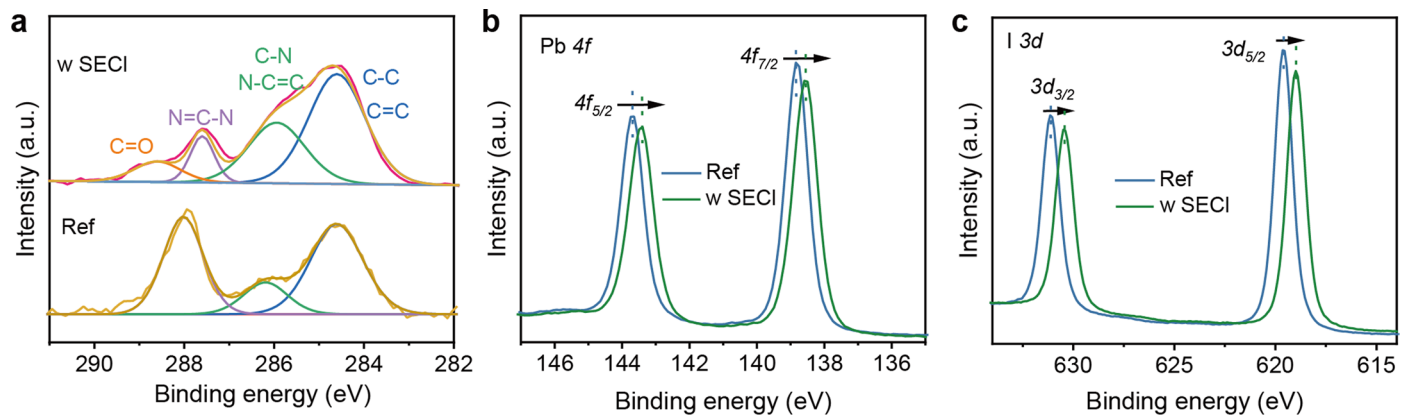
**Reprints and permissions information** is available at [www.nature.com/reprints](http://www.nature.com/reprints).



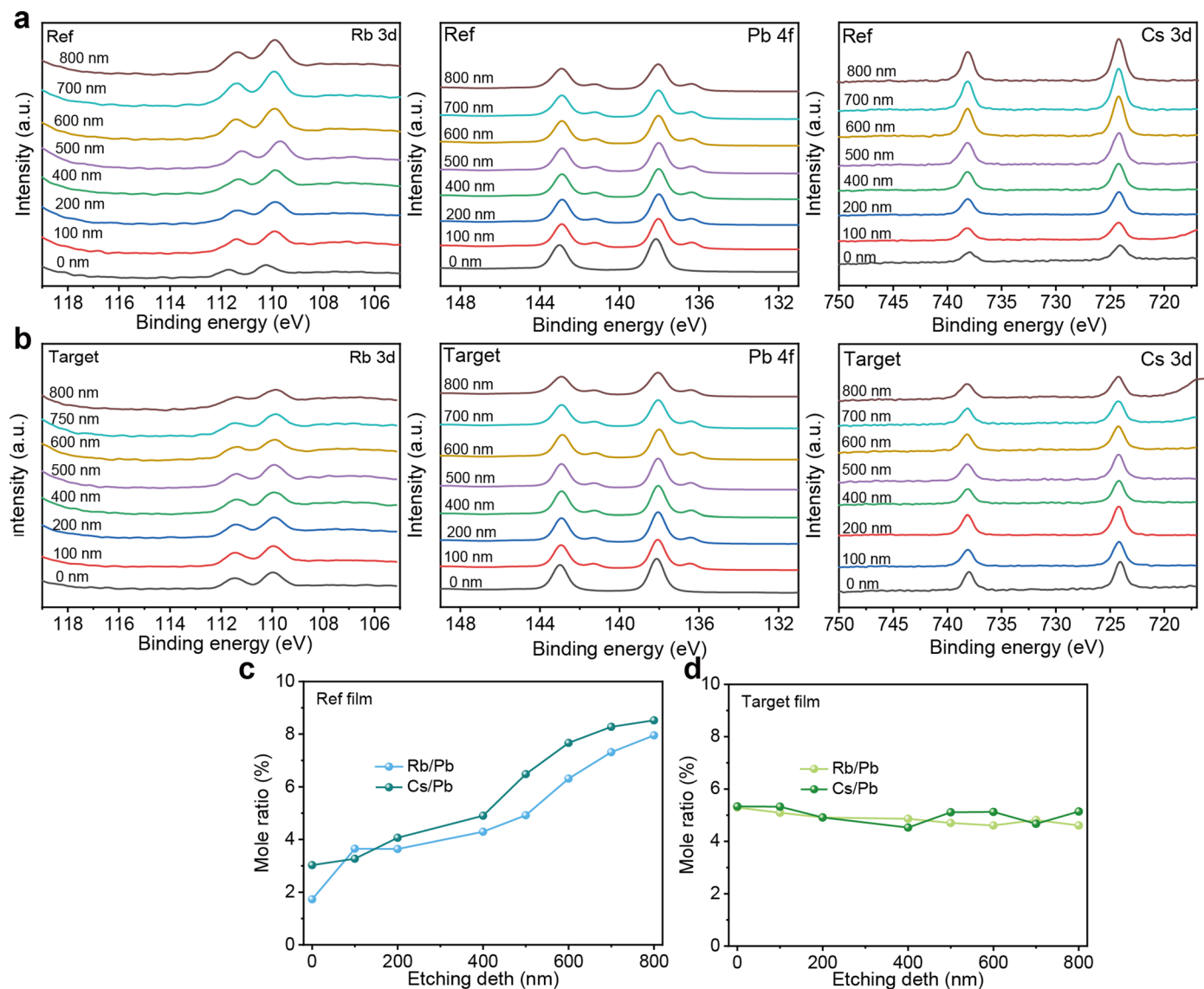
**Extended Data Fig. 1** | TG spectrum of SECl powders (7.591 mg). The powders decompose at a temperature of around 165.4 °C.



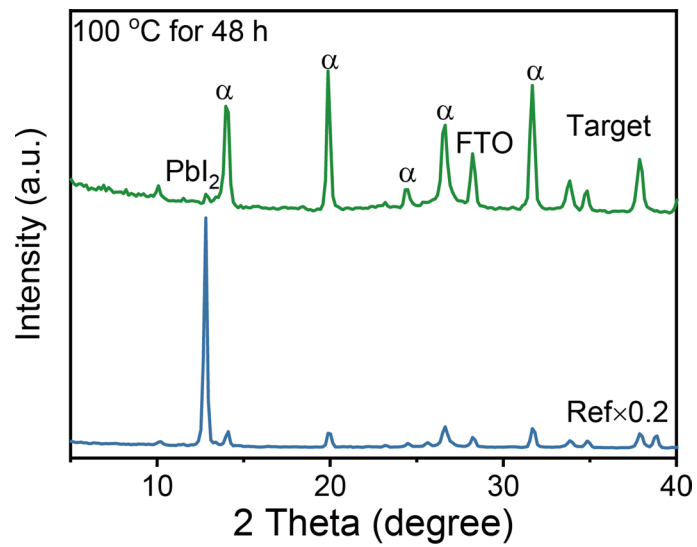
**Extended Data Fig. 2 | XRD patterns of the films with different SECl concentrations.** The film with 2 mg/mL SECl shows the strongest XRD intensity among all the conditions.



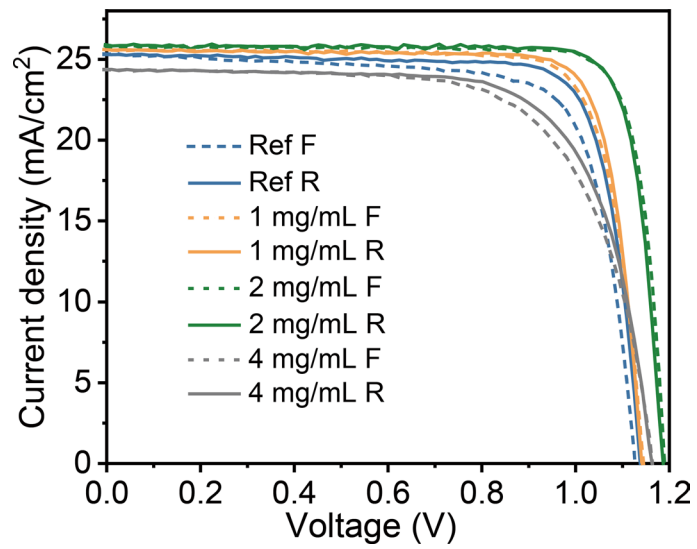
**Extended Data Fig. 3 | XPS spectra of the Ref and Target films.** In comparison to the Ref, the Target shows an obvious peak of -C = O (a), confirming the existence of SECI in the annealed film. The chemical shifts of the Pb 4f (b) and I 3d (c) binding energies in the Target film reflect the change in the distribution of A-site cations.



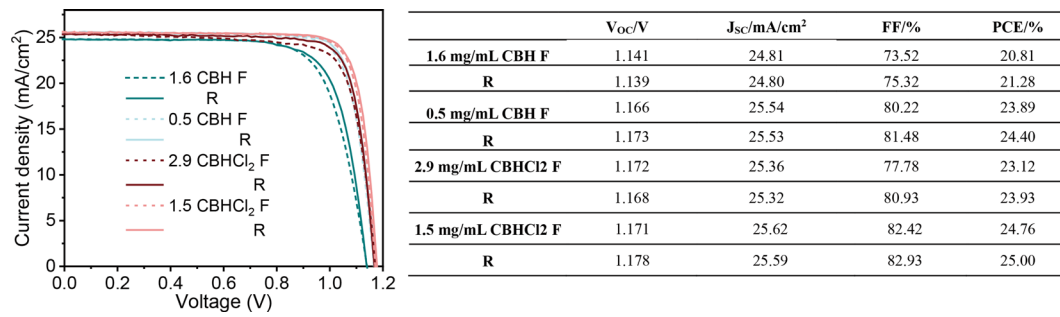
**Extended Data Fig. 4 | XPS depth profiles of the Ref and Target films.** (a), (b) XPS spectra of Rb, Pb, and Cs at different depths in the Ref and Target films. (c), (d) extracted Rb/Pb and Cs/Pb ratios at different depths in the Ref and Target films.



**Extended Data Fig. 5 | Thermal stability of the perovskite films.** XRD patterns of the aged Ref and Target perovskite films.



**Extended Data Fig. 6** | J-V curves of the p-i-n PSCs with different SECI concentrations. The detailed parameters are listed in Extended Data Table 1.



**Extended Data Fig. 7 | Photovoltaic performances with CBH and CBHCl<sub>2</sub> additives.** J-V curves and PV parameters of p-i-n PSCs with two different amounts of CBH and CBHCl<sub>2</sub>.

Extended Data Table 1 | Photovoltaic parameters of the p-i-n PSCs with different SECl concentrations

	$V_{oc}/V$	$J_{sc}/mA/cm^2$	FF/%	PCE/%
<b>Ref F</b>	1.127	25.33	75.57	21.57
<b>R</b>	1.138	25.32	79.96	23.04
<b>1 mg/mL F</b>	1.145	25.61	80.161	23.51
<b>R</b>	1.142	25.63	82.136	24.04
<b>2 mg/mL F</b>	1.187	25.79	84.62	25.90
<b>R</b>	1.185	25.78	85.51	26.12
<b>4 mg/mL F</b>	1.164	24.35	68.211	19.33
<b>R</b>	1.162	24.38	71.136	20.15

## Solar Cells Reporting Summary

Nature Portfolio wishes to improve the reproducibility of the work that we publish. This form is intended for publication with all accepted papers reporting the characterization of photovoltaic devices and provides structure for consistency and transparency in reporting. Some list items might not apply to an individual manuscript, but all fields must be completed for clarity.

For further information on Nature Research policies, including our [data availability policy](#), see [Authors & Referees](#).

### ► Experimental design

Please check the following details are reported in the manuscript, and provide a brief description or explanation where applicable.

#### 1. Dimensions

Area of the tested solar cells	<input checked="" type="checkbox"/> Yes	0.049 cm <sup>2</sup> mask for unit cells and 1.21 cm <sup>2</sup> mask for large-area devices
	<input type="checkbox"/> No	<i>Explain why this information is not reported/not relevant.</i>
Method used to determine the device area	<input checked="" type="checkbox"/> Yes	The aperture shade masks are used for photovoltaic performance collections
	<input type="checkbox"/> No	<i>Explain why this information is not reported/not relevant.</i>

#### 2. Current-voltage characterization

Current density-voltage (J-V) plots in both forward and backward direction	<input checked="" type="checkbox"/> Yes	Figs. 4a and 4e, Supplementary Figs. 21, 22, 24 and 25
	<input type="checkbox"/> No	
Voltage scan conditions	<input checked="" type="checkbox"/> Yes	The J-V curves were measured from 1.4 V to -0.2 V with a scanning rate of 100 mV/s (voltage step of 10 mV and delay time of 100 ms)
	<input type="checkbox"/> No	<i>Explain why this information is not reported/not relevant.</i>
Test environment	<input checked="" type="checkbox"/> Yes	Encapsulated devices were measured in ambient condition at room temperature with the controlled relative humidity range from 30% to 50%
	<input type="checkbox"/> No	<i>Explain why this information is not reported/not relevant.</i>
Protocol for preconditioning of the device before its characterization	<input checked="" type="checkbox"/> Yes	No preconditioning was used for the unit cell and large-area devices. The mini-modules need be pre-heated at 100 °C for 2 min before measuring (method),
	<input type="checkbox"/> No	<i>Explain why this information is not reported/not relevant.</i>
Stability of the J-V characteristic	<input checked="" type="checkbox"/> Yes	Maximum power point was verified (Supplementary Fig. 26).
	<input type="checkbox"/> No	<i>Explain why this information is not reported/not relevant.</i>

#### 3. Hysteresis or any other unusual behaviour

Description of the unusual behaviour observed during the characterization	<input type="checkbox"/> Yes	<i>Provide a description of hysteresis or any other unusual behaviour observed during the characterization.</i>
	<input checked="" type="checkbox"/> No	We observed negligible hysteresis in our devices
Related experimental data	<input checked="" type="checkbox"/> Yes	Figs. 4a, 4e, Supplementary Figs. 21, 22, 24 and 25
	<input type="checkbox"/> No	<i>Explain why this information is not reported/not relevant.</i>

#### 4. Efficiency

External quantum efficiency (EQE) or incident photons to current efficiency (IPCE)	<input checked="" type="checkbox"/> Yes	Fig. 4b and Supplementary Fig. 28
	<input type="checkbox"/> No	<i>Explain why this information is not reported/not relevant.</i>
A comparison between the integrated response under the standard reference spectrum and the response measure under the simulator	<input checked="" type="checkbox"/> Yes	Certified results in Fig. 4b and Supplementary Figs. 22
	<input type="checkbox"/> No	<i>Explain why this information is not reported/not relevant.</i>

For tandem solar cells, the bias illumination and bias voltage used for each subcell

- Yes  
 No

*Provide a description of the measurement conditions.*

No tandem solar cells were fabricated in this work.

## 5. Calibration

Light source and reference cell or sensor used for the characterization

- Yes  
 No

Characteristics of films and devices: The standard solar cells (certified by NREL) were used to check the spectra of solar simulator and EQE equipments.

*Explain why this information is not reported/not relevant.*

Confirmation that the reference cell was calibrated and certified

- Yes  
 No

The standard solar cell was used as the reference for calibration

*Explain why this information is not reported/not relevant.*

Calculation of spectral mismatch between the reference cell and the devices under test

- Yes  
 No

The spectral mismatch is negligible as the difference between the Jsc and EQE results

*Explain why this information is not reported/not relevant.*

## 6. Mask/aperture

Size of the mask/aperture used during testing

- Yes  
 No

Characteristics of films and devices: 0.049 cm<sup>2</sup> mask for unit cells and 1.21 cm<sup>2</sup> mask for large-area devices

*Explain why this information is not reported/not relevant.*

Variation of the measured short-circuit current density with the mask/aperture area

- Yes  
 No

Fig. 4c and Supplementary Figs. 23, 27 and 30

*Explain why this information is not reported/not relevant.*

## 7. Performance certification

Identity of the independent certification laboratory that confirmed the photovoltaic performance

- Yes  
 No

Fig. 4b and Supplementary Figs. 22, certified J-V from NREL with quasi-steady-state efficiency of 25.33%

*Explain why this information is not reported/not relevant.*

A copy of any certificate(s)

- Yes  
 No

Supplementary Figs. 22

*Explain why this information is not reported/not relevant.*

## 8. Statistics

Number of solar cells tested

- Yes  
 No

30 separated devices for each composition were fabricated ( Supplementary Figs. 23, 27 and 30).

*Explain why this information is not reported/not relevant.*

Statistical analysis of the device performance

- Yes  
 No

Supplementary Table 1

*Explain why this information is not reported/not relevant.*

## 9. Long-term stability analysis

Type of analysis, bias conditions and environmental conditions

- Yes  
 No

Characteristics of films and devices: The room-temperature MPPT of the encapsulated unit, large-area and mini-module cells were tested at the custom-built system with the Keithly 2400 and simulated AM 1.5 illumination at 35 C. High-temperature MPPT was measured on the oven with controlled temperature of 85 C. Both measurements were conducted at ambient condition with the humidity around 40% to 60%.

*Explain why this information is not reported/not relevant.*